

A multi-methodological study of kurnakovite: A potential B-rich aggregate

G. DIEGO GATTA^{1,*}, ALESSANDRO GUASTONI², PAOLO LOTTI¹, GIORGIO GUASTELLA³,
OSCAR FABELO⁴, AND MARIA TERESA FERNANDEZ-DIAZ⁴

¹Dipartimento di Scienze della Terra, Università degli Studi di Milano, Via Botticelli 23, I-20133 Milano, Italy. Orcid 0000-0001-8348-7181

²Dipartimento di Geoscienze, Università degli Studi di Padova, Via G. Gradenigo 6, I-35131, Padova, Italy

³Agenzia delle Dogane e dei Monopoli, Direzione Regionale per la Lombardia, Laboratorio e Servizi Chimici, Via Marco Bruto 14, I-20138 Milan, Italy

⁴Institut Laue-Langevin, 71 Avenue des Martyrs, F-38000 Grenoble, France

ABSTRACT

The crystal structure and crystal chemistry of kurnakovite from Kramer Deposit (Kern County, California), ideally $\text{MgB}_3\text{O}_3(\text{OH})_5 \cdot 5\text{H}_2\text{O}$, were investigated by single-crystal neutron diffraction (data collected at 293 and 20 K) and by a series of analytical techniques aimed to determine its chemical composition. The concentration of more than 50 elements was measured. The empirical formula of the sample used in this study is $\text{Mg}_{0.99}(\text{Si}_{0.01}\text{B}_{3.00})_{\Sigma 3.01}\text{O}_{3.00}(\text{OH})_5 \cdot 4.98\text{H}_2\text{O}$. The fraction of rare earth elements (REE) and other minor elements are, overall, insignificant. Even the content of fluorine, as a potential OH-group substituent, is insignificant (i.e., ~ 0.008 wt%). The neutron structure model obtained in this study, based on intensity data collected at 293 and 20 K, shows that the structure of kurnakovite contains: $[\text{BO}_2(\text{OH})]$ -groups in planar-triangular coordination (with the B-ions in sp^2 electronic configuration), $[\text{BO}_2(\text{OH})_2]$ -groups in tetrahedral coordination (with the B-ions in sp^3 electronic configuration), and $\text{Mg}(\text{OH})_2(\text{H}_2\text{O})_4$ -octahedra, connected into (neutral) $\text{Mg}(\text{H}_2\text{O})_4\text{B}_3\text{O}_3(\text{OH})_5$ units forming infinite chains running along [001]. Chains are mutually connected to give the tri-dimensional structure only via hydrogen bonding, and extra-chains “zeolitic” H_2O molecules are also involved as “bridging molecules.” All the oxygen sites in the structure of kurnakovite are involved in hydrogen bonding, as *donors* or as *acceptors*.

The principal implications of these results are: (1) kurnakovite does not act as a geochemical trap of industrially relevant elements (e.g., Li, Be, or REE), (2) the almost ideal composition makes kurnakovite a potentially good B-rich aggregate in concretes (for example, used for the production of radiation-shielding materials for the elevated ability of ^{10}B to absorb thermal neutrons), which avoids the risk to release undesirable elements, for example sodium, that could promote deleterious reactions for the durability of cements.

Keywords: Kurnakovite, borates, single-crystal neutron diffraction, crystal chemistry, hydrogen bonding, B-rich aggregate

INTRODUCTION

Kurnakovite, with the ideal chemical formula $\text{MgB}_3\text{O}_3(\text{OH})_5 \cdot 5\text{H}_2\text{O}$, is a complex hydrous borate mineral found as a common constituent of borate deposits, along with borax [ideally $\text{Na}_2(\text{B}_4\text{O}_5)(\text{OH})_4 \cdot 8\text{H}_2\text{O}$] and ulexite {ideally $\text{NaCa}[\text{B}_5\text{O}_6(\text{OH})_6] \cdot 5\text{H}_2\text{O}$ }. Natural borates represent the most important source of boron, which is an important geochemical marker for petrogenetic processes (especially in pegmatitic and granitic systems) and a strategic element for technological materials (e.g., to lower melting temperatures and melt viscosities in silicate glass systems), but they are also being used for the production of radiation-shielding materials for the elevated ability of ^{10}B to absorb thermal neutrons. More specifically, the most important use is to absorb neutrons emitted by nuclear reactors for energy production, scientific research, or medical applications, which promotes the development of suitable materi-

als able to shield from harmful radiations. Approximately 20% of natural boron is ^{10}B , which shows a high capacity to absorb thermal neutrons due to its high cross section for the $^{10}\text{B}(n,\alpha)^7\text{Li}$ reaction (~ 3840 barns; Carter et al. 1953; Palmer and Swihart 1996; Rauch and Waschkowski 2002). Borax and ulexite have been objects of investigation to produce B-rich aggregates in concretes. However, these two minerals have proved they induce a drastic effect on setting and hardening, coupled with a drastic lowering of strength development and durability of concretes (e.g., Glinicki et al. 2018). In addition, these minerals dissolve into the paste, releasing sodium, that could potentially promote deleterious reactions for the durability of Portland cements. On the other hand, the use of the most stable compounds, for example like the synthetic B_4C or B-mullites, is not environmentally and economically sustainable (Okuno et al. 2009; Gatta et al. 2013; Di Julio et al. 2017). In the framework of a long-term project to select new potential substituents of borax and ulexite as B-bearing aggregates, using a multi-methodological approach we have

* E-mail: diego.gatta@unimi.it

recently investigated the crystal chemistry, the stability at high and low temperature (Lotti et al. 2018, 2019), and at high pressure (Lotti et al. 2017) of colemanite [ideally $\text{CaB}_3\text{O}_4(\text{OH})_3 \cdot \text{H}_2\text{O}$]. We now extend our investigation to kurnakovite, a Na-free borate with $\text{B}_2\text{O}_3 \approx 37$ wt%, starting with a careful crystal-chemical investigation, which will be followed by experiments on its chemical and P - T stability.

Only a few studies were devoted to this mineral and to its dimorph inderite. After preliminary (and incomplete) data about the crystallographic features of kurnakovite (Petch et al. 1962), its first structure model was reported by Razmanova et al. (1969), and later refined by Corazza (1974) on the basis of single-crystal X-ray Weissenberg data, in the space group $P\bar{1}$ with $a \approx 8.35$ Å, $b \approx 10.61$ Å, $c \approx 6.44$ Å, $\alpha \approx 98.8^\circ$, $\beta \approx 109.0^\circ$, $\gamma \approx 105.6^\circ$ ($V \approx 501.2$ Å³). No more recent structural refinements are reported in the literature. ¹¹B and ²⁵Mg NMR data and DFT calculations of the crystal structure of inderite and kurnakovite were recently reported by Zhou et al. (2012). Following the model of Corazza

(1974), the structure of kurnakovite contains: $[\text{BO}_2(\text{OH})]$ -groups in triangular coordination, $[\text{BO}_2(\text{OH})_2]$ -groups in tetrahedral coordination, and $\text{Mg}(\text{OH})_2(\text{H}_2\text{O})_4$ octahedra, connected into (neutral) $\text{Mg}(\text{H}_2\text{O})_4\text{B}_3\text{O}_3(\text{OH})_5$ units forming chains running along the $[001]$ direction (Fig. 1). “Zeolitic” H_2O molecules populate small cavities, hydrogen bonded to the aforementioned chains. The major difference between the dimorphs kurnakovite and inderite lies in the linkage of the $\text{Mg}(\text{H}_2\text{O})_4\text{B}_3\text{O}_3(\text{OH})_5$ unit: in inderite this unit consists of the triborate ring and $\text{Mg}(\text{OH})_2(\text{H}_2\text{O})_4$ octahedron sharing two OH groups, whereas in kurnakovite the unit is composed of alternating triborate rings and $\text{Mg}(\text{OH})_2(\text{H}_2\text{O})_4$ octahedra, sharing one oxygen atom to form infinite chains (Fig. 1).

The X-ray refinement model of Corazza (1974) provided the position of H-sites in the structure of kurnakovite and a general description of the hydrogen bonds acting as linkages between the $[001]$ -chains. No chemical analysis was performed on the investigated material by Corazza (1974), assuming the

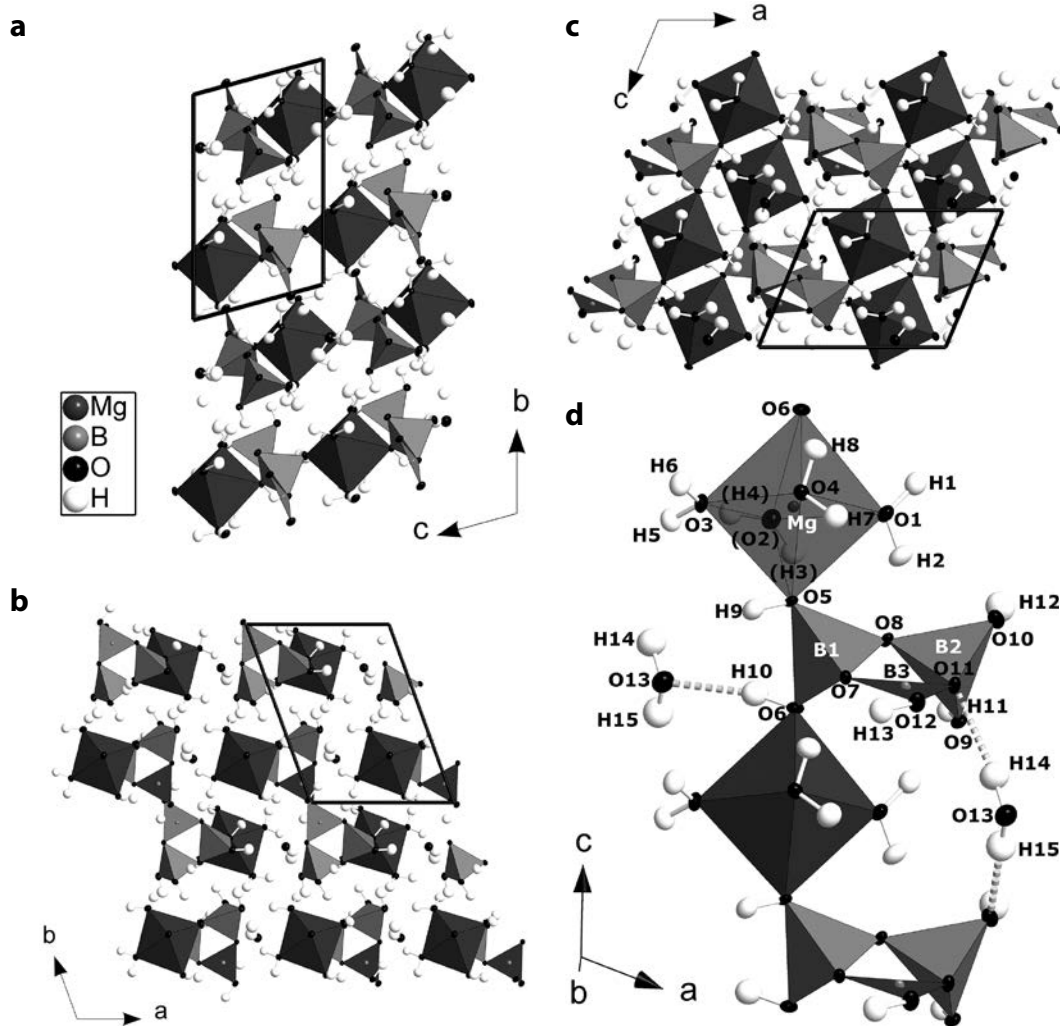


FIGURE 1. Three views of the crystal structure of kurnakovite along with the configuration of the $\text{Mg}(\text{H}_2\text{O})_4\text{B}_3\text{O}_3(\text{OH})_5$ units (forming infinite chains running along $[001]$), based on the neutron structure refinement of this study (intensity data collected at 293 K). Displacement ellipsoid probability factor: 50%.

ideal chemical composition of the mineral previously reported by Razmanova et al. (1969). Despite the general structure model appears to be consistent (in terms of bond distances and angles), the structure refinement of Corazza (1974) provides only a partial view of the H-bonding configuration, due to the limitation of the X-ray diffraction at that time. In addition, some differences between the structure model of Razmanova et al. (1969) and Corazza (1974) actually exist. Kurnakovite is one of the few minerals that contain hydroxyl groups, cation-coordinated H₂O molecules and “zeolitic” H₂O molecules, and therefore a model with an accurate location of the H-sites is necessary. In this light, and considering the expected important role played by the H-bonding network on the phase stability of kurnakovite (i.e., the overall H₂O content is ~48 wt%), the aim of the present study is a reinvestigation of the crystal structure and crystal chemistry of kurnakovite by single-crystal neutron diffraction at room and low temperature (20 K) along with a series of other analytical techniques [i.e., titrimetric analysis for the determination of B and Mg content, inductively coupled plasma atomic emission spectroscopy (ICP-AES) for REE and other minor elements, ion selective electrode for F, high-*T* mass loss for H₂O content]. The combination of these techniques is expected to provide:

- (1) an unambiguous location of all the proton sites and the description of the complex H-bonding network in the kurnakovite structure, along with its low-*T* induced rearrangement;
- (2) the anisotropic displacement parameters of all the atomic sites, including the H-sites;
- (3) a more robust description of B-coordination environment [e.g., aplanarity of the BO₂(OH)-group, tetrahedral distortion of the BO₂(OH)₂-groups];
- (4) a description of the crystal chemistry of this mineral based on modern analytical protocols, with a particular attention to the potential B- and Mg-substituents.

The neutron diffraction experiment at low *T* has been performed because the vibrational regime of protons at room temperature can give rise to some dynamic or static disorder, which is minimized at low *T*. We expect that the experimental findings of the present crystal-chemical investigation will be pivotal to fully understand the chemical and *P-T* stability of this mineral, even for its potential use as environmentally and economically sustainable (mineral) B-bearing aggregates in Portland, Sorel, or other types of cements.

SAMPLE DESCRIPTION AND OCCURRENCE

The sample of kurnakovite used in this study belongs to the collection of the Museum of Mineralogy of the University of Padova (Italy). A fragment of a large translucent crystal, measuring 20 cm as the maximum length and showing a combination of well-formed euhedral pinacoids, was used. The specimen was collected at the Kramer Deposit, Mohave desert, Kern County, California. In 1913, this boron deposit was accidentally discovered when a well was drilled for water in the Mohave desert, and it penetrated the bedrock beneath the alluvium reaching the colemanite-bearing stratigraphic layer (Noble 1926). The production of borax and other borates began in 1927 and continued until 1957 when the diggings changed to open pit quarry.

The geologic setting of the kurnakovite deposit is imperfectly known. The borate minerals, several hundred feet underground, occur in a complex clay series, underlain by igneous rocks composed by basaltic lavas, upper Miocene in age and overlain by a stratigraphic series of continental arkosic sands (Siefke 1991). The deposit has been dated as upper Miocene on the basis of mammalian fossils discovered above borates (Whistler 1984). The Kramer deposit consists of a lenticular mass of borax and subordinate ulexite, colemanite, kernite, and kurnakovite, measuring 1.6 km long, 0.8 wide, and up to 100 m thick. The bed of basaltic lava underlying the borate deposits is believed to have been poured out and to be indirectly the source of boron, which was derived from the hot springs and solfataras connected with the Tertiary volcanic activity. Tuffaceous clay beds, showing ripple marks as well, occur interbedded with borax (Obert and Long 1962).

More than 80 minerals have been reported occurring in the Kramer deposit including several borates as borax, colemanite, greigite, hydroboracite, inderite, inyoite, kernite, kurnakovite, meyerhofferite, probertite, searlesite, tinalconite, tunellite, and ulexite. No evidence of the most common evaporite minerals, like halite and gypsum, were found associated with primary borax and other borates beds (Schaller 1930; Morgan and Erd 1969; Puffer 1975).

EXPERIMENTAL METHODS

Titrimetric determination of boron

A mass of 80–100 mg of a sample of kurnakovite was placed in a 50 mL plastic test tube, along with 5 mL of water and 3 mL of hydrochloric acid 1 M; the plastic test tube was then covered and transferred in an ultrasound bath for 1–2 h. The resulting clear solution was transferred in a 200–300 mL beaker with water up to about 100 mL of the total solution. A combined glass electrode (InLab Routine Pro-Mettler Toledo) was immersed in the solution, and the pH was adjusted to 5.5–6.5 with solutions of HCl 0.1–1 M and NaOH 0.1–1 M. 5–6 g of mannitol were added and stirred until the complete dissolution of the solid. The solution was then titrated with NaOH 0.1 M up to pH 8.3–8.7. The content of acid titrated was entirely due to the presence of boric acid in solution, as the sample does not contain elements capable to hydrolyze the medium, or in general able to influence its acidity. The measured fraction of B₂O₃ was 37.3(3) wt%.

EDTA titrimetric determination of magnesium

A mass of 40–80 mg of mineral sample was placed in a 50 mL plastic test tube, along with 5 mL of water and 1 mL of hydrochloric acid 1 M; the plastic tube was covered with a lid and transferred in an ultrasound bath for 1–2 h. The resulting clear solution was transferred in a 300–400 mL beaker and diluted to 200 mL with water. 10 mL of buffer solution (pH 10 mixture ammonium chloride/ammonia) and 3–4 drops of Eriochrome black T solution (2 g/l in ethanol) were added. The solution was then titrated with a standard solution of EDTA (ethylenediaminetetraacetic acid) 0.01 M. The end point was reached when the reddish purple color of the solution was altered to blue. The total volume of EDTA used was assumed to be related to the average of the magnesium content of the sample. The obtained fraction of MgO was 14.3(2) wt%.

Determination of fluorine content

A mineral sample of 20 mg in mass was placed in a 50 mL plastic test tube, along with 5 mL of water and 3 mL of hydrochloric acid 1M; the plastic test tube was covered and transferred in an ultrasound bath for 1–2 h. 2–3 mL of Total Ionic Strength Adjustment Buffer (commercial solution TISAB III) was added to the clear solution and diluted to 20 mL with water. The F content was then determined using the perfectION Combination Fluoride Ion Selective Electrode (Mettler Toledo), adopting the method of standard addition. Solutions of fluorine from 0.1 to 5.0 mg/L were prepared by Certified Reference Material-CRM 1000 mg/L of fluorine. The resulting F fraction was 0.008 wt% (uncertainty not determined).

Determination of H₂O content by heating

A sample of 500–600 mg was placed in a quartz crucible with lid, and gradually heated in a muffle furnace from ambient temperature up to 800 °C. Assuming that the mass loss represents the total amount of H₂O, the estimated fraction of H₂O of the sample was 48.2(2) wt%.

Determination of minor elements by inductively coupled plasma atomic emission spectroscopy (ICP-AES)

All measurements were performed in axial view mode for REE and radial view mode for the other minor elements with a Perkin Elmer Optima 7000DV ICP-AES spectrometer.

Determination of REE concentration by ICP-AES. 50 mg of mineral sample was placed in a 50 mL plastic test tube, along with 5 mL of water and 3 mL of hydrochloric acid 1M; plastic test tube was covered and transferred in an ultrasound bath for 1–2 h. The resulting clear solution was then transferred and diluted with water in a 50 mL volumetric flask. A calibration protocol was performed with a blank solution and a series of solutions prepared with similar fractions of magnesium and boron as those of the sample under investigation and REE concentration from 0.001 to 0.050 mg/L for each element (using CRM multi-elemental standard mix for ICP). Results and instrumental parameters are listed in Table 1.

Determination of other minor elements concentration by ICP-AES. For the non-REE minor elements determination, two different protocols were used.

Protocol 1. 10–20 mg of mineral sample was placed in a 50 mL plastic test tube, along with 5 mL of water and 3 mL of hydrochloric acid 1M; the plastic test tube was covered and transferred in an ultrasound bath for 1–2 h. The resulting clear solution was transferred and diluted with water in a 25 mL volumetric flask containing 2.5 mL of scandium solution 100 mg/L as an internal standard. A calibration protocol was performed with a blank solution and a series of 5 solutions prepared with concentration from 0.05 to 1.0 mg/L for each element (using CRM multi-elemental standard mix for ICP).

Protocol 2. Decomposition by alkaline fusion of 10–20 mg of mineral sample in a platinum crucible with 100 mg of sodium carbonate or potassium carbonate in a muffle furnace at 1000 °C for 5 min, followed by dissolution in 10 mL of water and 1 mL of sulfuric acid 1M or 1 mL of hydrochloric acid 1M. The clear solution was then transferred and diluted with water in a 25 mL volumetric flask containing 2.5 mL of scandium solution 100 mg/L as an internal standard. A calibration protocol was performed with a blank solution and a series of 5 solutions prepared with concentration from 0.05 to 1.0 mg/L for each element (using CRM multi-elemental standard mix for ICP). Results and instrumental parameters are listed in Table 2.

A representative chemical analysis of kurnakovite from Kramer Deposit is given in Table 3, and its empirical formula was recalculated on the basis of 13 anions.

Single-crystal neutron diffraction

The first set of single-crystal neutron diffraction data was collected at room temperature from a fragment of kurnakovite (~3 × 4 × 4 mm³) on the four-circle diffractometer D9 at the Institut Laue-Langevin (ILL), Grenoble. The wavelength of 0.8377(1) Å, obtained from a Cu(220) monochromator, and a small two-dimensional area detector were used. The measurement strategy consisted of a series of ω-scans or ω-2θ scans for low and high-Q reflections, respectively. The reflections were collected by varying the ω-range as a function of the instrument resolution curve. A total number of 2252 reflections were collected. The integration, background, and Lorentz factor correction of the scans were done with the program RACER (Wilkinson et al. 1988). The lattice was found to be metrically triclinic, as previously reported by Corazza (1974).

A further set of data from the same crystal was collected at room temperature on the monochromatic four-circle diffractometer D19 at ILL. The wavelength used was 1.4538(1) Å, provided by a flat Cu(220) monochromator (at 2θ_M = 69.91° take-off angle). The measurement strategy consisted of a series of ω-scans with steps of 0.07° at different γ and φ positions, with 2123 collected reflections. The data collection was performed using the Multi-Detector Acquisition Data Software (MAD) from ILL. Indexing and unit-cell determination were done by using PFIND and DIRAX programs (Duisenberg 1992). The integration of the raw data and refinement of the UB-matrix, including the off-sets, were done using RETREAT and RAFFD19 programs, respectively, along with the Lorentz correction of the intensities (Wilkinson et al. 1988). The lattice was found to be metrically triclinic, according to the first data set collected on D9. The absorption correction was carried out using D19abs program (Matthewman et al. 1982).

Considering the two sets of data at room temperature (i.e., 293 K), a total of 3805 independent reflections were obtained after merging (with $-11 \leq h \leq +10$,

$-14 \leq k \leq +13$ and $-7 \leq l \leq +9$, Laue group $\bar{1}$, $R_{\text{Friedel}} = 0.0583$; Supplemental¹ Table S1), out of which 3574 with $F_o > 4\sigma(F_o)$, with $d_{\text{min}} = 0.71$ Å. Further details pertaining to the data collection strategy are listed in Supplemental¹ Table S1.

A second data set was collected on the four-circle diffractometer D19 with Cu(331)-monochromated radiation (take-off angle 2θ_M = 70°), providing neutrons with a wavelength of 0.9449(1) Å. The same crystal of kurnakovite used for the room-temperature experiments was glued on a vanadium pin and placed on a close-circuit displacer device operated at 20.0(5) K (Archer and Lehmann 1986).

TABLE 1. REE concentrations by ICP-AES (see text for details)

	%m/m	ICP-AES (nm)	LOD	LOQ
Ce ₂ O ₃	<LOD	413.764	0.003	0.01
Dy ₂ O ₃	<LOD	353.170	0.0001	0.0003
Er ₂ O ₃	<LOD	369.265	0.002	0.007
Eu ₂ O ₃	<LOD	381.967	0.0001	0.0003
Gd ₂ O ₃	<LOD	342.247	0.0003	0.001
Ho ₂ O ₃	<LOD	345.600	0.0001	0.0003
La ₂ O ₃	0.0003	398.852	0.0001	0.0003
La ₂ O ₃	>LOD	408.672	0.0002	0.0006
Lu ₂ O ₃	<LOD	261.542	0.0002	0.0006
Nd ₂ O ₃	<LOD	406.109	0.0002	0.0006
Pr ₂ O ₃	<LOD	390.844	0.0002	0.0006
Sm ₂ O ₃	<LOD	359.260	0.0005	0.002
Sc ₂ O ₃	<LOD	361.383	0.0005	0.002
Tb ₂ O ₃	<LOD	350.917	0.0005	0.002
Tm ₂ O ₃	<LOD	313.126	0.004	0.015
Yb ₂ O ₃	<LOD	328.937	0.0001	0.0003
Y ₂ O ₃	<LOD	371.029	0.0001	0.0003
ThO ₂	<LOD	283.730	0.001	0.004
UO ₂	<LOD	385.958	0.01	0.04

Note: LOD = Limit of detection (3σ); LOQ = Limit of quantification (10σ).

TABLE 2. Concentrations of other minor elements by ICP-AES (see text for details)

	%m/m	ICP-AES (nm)		%m/m	ICP-AES (nm)
Li ₂ O	<0.01	670.784	NiO	<0.01	231.604
Na ₂ O	<0.01	589.592	CuO	<0.01	327.393
K ₂ O	<0.01	766.490	Ag ₂ O	<0.01	328.068
Rb ₂ O	<0.02	780.023	ZnO	<0.01	206.200
Cs ₂ O	<0.02	455.531	CdO	<0.01	228.802
BeO	<0.01	313.107	Al ₂ O ₃	<0.02	396.153
CaO	0.03	317.933	Tl ₂ O	<0.02	190.801
BaO	<0.02	233.527	PbO	<0.05	220.353
TiO ₂	<0.01	334.940	P ₂ O ₅	<0.02	213.617
ZrO ₂	<0.01	343.823	As ₂ O ₃	<0.02	193.696
V ₂ O ₅	<0.02	292.464	Sb ₂ O ₃	<0.02	206.836
Cr ₂ O ₃	<0.01	267.716	Bi ₂ O ₃	<0.02	223.061
MoO ₃	<0.02	202.031	SiO ₂	0.23	251.611
MnO	<0.01	257.610	SrO	<0.01	407.771
Fe ₂ O ₃	0.03	238.204	B ₂ O ₃ *	/	249.677
CoO	<0.01	228.616	MgO*	/	285.213

* Data were not reproducible and therefore discarded.

TABLE 3. Representative chemical analysis of kurnakovite from Kramer Deposit (Kern County, California), with (left side) and without (right side) the SiO₂ fraction (see text for details), and empirical formulas recalculated on the basis of 13 anions

Oxides	wt%	e.s.d.	Oxides	wt%
B ₂ O ₃	37.3	0.3	B ₂ O ₃	37.30
MgO	14.3	0.2	MgO	14.30
SiO ₂	0.23	n.d.	CaO	0.03
CaO	0.03	n.d.	Fe ₂ O ₃	0.03
Fe ₂ O ₃	0.03	n.d.	H ₂ O	48.20
H ₂ O	48.2	0.2		
Total	100.09		Total	99.86

Elements	apfu	Elements	apfu
B ³⁺	3.00	B ³⁺	3.00
Si ⁴⁺	0.01	Mg ²⁺	0.99
Mg ²⁺	0.99	Ca ²⁺	0.00
Ca ²⁺	0.00	Fe ³⁺	0.00
Fe ³⁺	0.00	H ⁺	15.00
H ⁺	14.97		

Empirical formula	Empirical formula
Mg _{0.99} (Si _{0.01} B _{3.00}) _{23.01} O _{3.00} (OH) ₅ ·4.98H ₂ O	Mg _{0.99} B _{3.00} O _{3.00} (OH) ₅ ·5.00H ₂ O

The measurement strategy consisted of ω scans of 64 or 79° with steps of 0.07° at different χ and ϕ positions. A total of 25 ω -scans were collected to complete almost half-Ewald sphere. Similarly, the data collection was performed using the MAD software from ILL, indexing and unit-cell metrical determination were done using PFIND and DIRAX programs, and integration of the raw data and refinement of the UB-matrix were done using RETREAT and RAFD19 programs. Even at low T , the lattice was found to be metrically triclinic, without any significant variation with respect to the unit-cell configuration obtained at room temperature. A total of 10334 reflections were integrated (with $-15 \leq h \leq +15$, $-5 \leq k \leq +18$, and $-11 \leq l \leq +11$, Laue group -1 , $R_{\text{friedel}} = 0.0536$, Supplemental¹ Table S1), out of which 5278 with $F_o > 4\sigma(F_o)$, with $d_{\text{min}} = 0.54 \text{ \AA}$. Further details pertaining to the data collection strategy are listed in Supplemental¹ Table S1.

Both the neutron intensity data sets (i.e., collected at 293 and 20 K) were processed with the program *E-STATISTICS*, implemented in the WinGX package (Farrugia 1999). The Wilson plot and the statistics of distributions of the normalized structure factors (E values) suggested that the structure of kurnakovite is centrosymmetric at >75% likelihood. Anisotropic crystal-structure refinements, based on the intensity data collected at room and low T , were conducted in the

space group $\bar{P}1$ using the SHELXL-97 software (Sheldrick 1997, 2008), starting from the structure model of Corazza (1974), without any H atom. The neutron scattering lengths of Mg, B, O, and H were taken from Sears (1986). Secondary isotropic extinction effect was corrected according to the formalism of Larson (1967). For both the refinements (i.e., 293 and 20 K), convergence was rapidly achieved after the first cycles, with a series of intense negative residual peaks in the final difference-Fourier map of the nuclear density, assigned to the H sites in the next cycles (i.e., H has a negative neutron scattering length). Shape and magnitude of the minima in the difference-Fourier maps of the nuclear density showed no evidence of positional or dynamic disorder of the H sites. At the end of the refinements [with $R_i(F) = 0.0693$ at 293 K, for 3574 obs/291par; $R_i(F) = 0.0415$ at 20 K, for 5278 obs/275par, Supplemental¹ Table S1], the variance-covariance matrix showed no significant correlation among the refined variables. In addition, all variable parameters converged with all the principal mean-square atomic displacement parameters positive, including those for the H sites. Further details pertaining to structure refinement strategy are given in Supplemental¹ Table S1. Atomic coordinates and displacement parameters are listed in Supplemental¹ Tables S2 and S3; selected interatomic distances and angles are given in Table 4.

TABLE 4. Relevant bond distances (Å) and angles (°) based on the neutron structure refinements

T = 293 K					
Mg-O1	2.014(3)	O8-B2-O9	111.4(2)	O5-H9	0.962(3)
Mg-O2	2.088(3)	O8-B2-O10	109.8(2)	O5-H9*	0.9796
Mg-O3	2.027(2)	O9-B2-O10	110.3(1)	O5-O4	2.876(2)
Mg-O4	2.145(3)	O8-B2-O11	111.4(1)	H9-O4	1.916(3)
Mg-O5	2.090(2)	O9-B2-O11	107.6(2)	O5-H9-O4	174.2(4)
Mg-O6	2.120(2)	O10-B2-O11	106.2(2)		
				O6-H10	0.965(6)
B1-O5	1.465(2)	O11-B3-O7	122.8(2)	O6-H10*	0.9904
B1-O6	1.502(2)	O11-B3-O12	117.2(2)	O6-O13	3.015(3)
B1-O7	1.512(3)	O7-B3-O12	120.0(2)	H10-O13	2.064(6)
B1-O8	1.445(2)			O6-H10-O13	167.7(5)
		O1-H2	0.969(5)		
B2-O8	1.458(2)	O1-H2*	0.9806	O9-H11	0.976(5)
B2-O9	1.477(2)	O1-O8	2.727(3)	O9-H11*	0.9914
B2-O10	1.478(3)	H2-O8	1.840(5)	O9-O8	2.759(3)
B2-O11	1.483(3)	O1-H2-O8	150.8(4)	H11-O8	1.783(5)
				O9-H1-O8	176.8(4)
B3-O7	1.370(2)	O2-H4	0.968(5)		
B3-O11	1.361(2)	O2-H4*	0.9818	O10-H12	0.930(6)
B3-O12	1.378(3)	O2-O10	2.798(3)	O10-H12*	0.9609
		H4-O10	1.842(5)	O10-O6	3.263(3)
O1-Mg-O3	176.7(1)	O2-H4-O10	168.7(5)	H12-O6	2.385(6)
O1-Mg-O2	95.6(1)	O2-H3	0.971(5)	O10-H12-O6	157.3(5)
O3-Mg-O2	86.3(1)	O2-H3*	0.9838	O10-O2	3.070(3)
O1-Mg-O5	88.5(1)	O2-O9	2.761(3)	H12-O2	2.483(5)
O3-Mg-O5	88.7(1)	H3-O9	1.835(5)	O10-H12-O2	121.2(4)
O2-Mg-O5	93.1(1)	O2-H3-O9	158.4(4)		
O1-Mg-O6	88.9(1)	H3-O2-H4	111.3(3)	O12-H13	0.967(6)
O3-Mg-O6	93.8(1)			O12-H13*	0.9901
O2-Mg-O6	91.3(1)	O3-H5	0.967(5)	O12-O13	2.859(6)
O5-Mg-O6	175.1(1)	O3-H5*	0.9778	H13-O13	1.895(5)
O1-Mg-O4	93.2(1)	O3-O11	2.705(3)	O12-H13-O13	174.2(4)
O3-Mg-O4	84.9(1)	H5-O11	1.741(4)		
O2-Mg-O4	171.2(1)	O3-H5-O11	174.5(4)	O13-H14	0.941(7)
O5-Mg-O4	87.1(1)	O3-H6	0.964(4)	O13-H14*	0.9642
O6-Mg-O4	88.9(1)	O3-H6*	0.9786	O13-O11	3.031(4)
		O3-O7	2.776(3)	H14-O11	2.149(7)
		H6-O7	1.815(4)	O13-H14-O11	155.7(5)
O8-B1-O5	108.4(2)	O3-H6-O7	174.1(4)	O13-H15	0.961(7)
O8-B1-O6	114.1(1)	H5-O3-H6	108.9(3)	O13-H15*	0.9869
O5-B1-O6	108.8(2)			O13-O10	2.899(4)
O8-B1-O7	110.3(2)			H15-O10	1.948(7)
O5-B1-O7	108.9(1)	O4-H8	0.970(4)	O13-H15-O10	170.2(5)
O6-B1-O7	106.2(2)	O4-H8*	0.9886	H14-O13-H15	110.9(5)
		O4-O7	2.705(2)		
		H8-O7	1.773(4)		
		O4-H8-O7	159.9(4)		
		O4-H7	0.979(6)		
		O4-H7*	0.9988		
		O4-O12	2.842(3)		
		H7-O12	1.875(6)		
		O4-H7-O12	169.0(5)		
		H8-O4-H7	105.2(4)		

TABLE 4.—CONTINUED

T = 20 K					
Mg-O1	2.0077(7)	O8-B2-O9	111.43(4)	O5-H9	0.970(1)
Mg-O2	2.0777(8)	O8-B2-O10	110.05(4)	O5-H9*	0.9887
Mg-O3	2.0150(7)	O9-B2-O10	111.14(4)	O5-O4	2.840(1)
Mg-O4	2.1313(8)	O8-B2-O11	111.50(4)	H9-O4	1.872(1)
Mg-O5	2.0690(6)	O9-B2-O11	107.36(4)	O5-H9-O4	174.8(1)
Mg-O6	2.0987(6)	O10-B2-O11	105.18(4)		
				O6-H10	0.969(2)
B1-O5	1.4616(7)	O11-B3-O7	123.02(5)	O6-H10*	0.9880
B1-O6	1.4940(7)	O11-B3-O12	116.84(5)	O6-O13	2.959(1)
B1-O7	1.5091(7)	O7-B3-O12	120.13(5)	H10-O13	2.008(1)
B1-O8	1.4383(7)			O6-H10-O13	166.7(1)
		O1-H2	0.969(2)		
B2-O8	1.4566(7)	O1-H2*	0.9880	O9-H11	0.985(2)
B2-O9	1.4739(7)	O1-O8	2.715(1)	O9-H11*	1.0003
B2-O10	1.4794(7)	H2-O8	1.826(2)	O9-O8	2.738(1)
B2-O11	1.4825(7)	O1-H2-O8	151.0(1)	H11-O8	1.753(2)
				O9-H11-O8	177.6(1)
B3-O7	1.3638(7)	O2-H4	0.978(2)		
B3-O11	1.3605(7)	O2-H4*	0.9951	O10-H12	0.961(2)
B3-O12	1.3766(7)	O2-O10	2.768(1)	O10-H12*	0.9842
		H4-O10	1.803(1)	O10-O6	3.312(1)
O1-Mg-O3	176.33(3)	O2-H4-O10	168.5(2)	H12-O6	2.406(2)
O1-Mg-O2	95.30(3)	O2-H3	0.976(2)	O10-H12-O6	156.9(1)
O3-Mg-O2	86.53(3)	O2-H3*	0.9951	O10-O2	3.004(1)
O1-Mg-O5	88.56(3)	O2-O9	2.731(1)	H12-O2	2.381(1)
O3-Mg-O5	88.16(3)	H3-O9	1.801(2)	O10-H12-O2	122.0(1)
O2-Mg-O5	93.43(3)	O2-H3-O9	158.1(2)		
O1-Mg-O6	89.70(3)	H3-O2-H4	110.9(1)	O12-H13	0.963(2)
O3-Mg-O6	93.45(3)			O12-H13*	0.9859
O2-Mg-O6	90.85(3)	O3-H5	0.974(2)	O12-O13	2.816(3)
O5-Mg-O6	175.52(4)	O3-H5*	0.9913	H13-O13	1.840(2)
O1-Mg-O4	93.04(3)	O3-O11	2.693(1)	O12-H13-O13	174.2(2)
O3-Mg-O4	85.16(3)	H5-O11	1.722(2)		
O2-Mg-O4	171.66(3)	O3-H5-O11	174.6(1)	O13-H14	0.963(2)
O5-Mg-O4	86.99(3)	O3-H6	0.972(2)	O13-H14*	0.9859
O6-Mg-O4	88.98(3)	O3-H6*	0.9903	O13-O11	3.003(1)
		O3-O7	2.747(1)	H14-O11	2.103(2)
		H6-O7	1.777(2)	O13-H14-O11	155.0(2)
O8-B1-O5	108.36(4)	O3-H6-O7	174.9(1)	O13-H15	0.976(2)
O8-B1-O6	114.23(5)	H5-O3-H6	108.4(1)	O13-H15*	0.9949
O5-B1-O6	108.85(4)			O13-O10	2.837(1)
O8-B1-O7	110.16(4)			H15-O10	1.875(2)
O5-B1-O7	108.91(4)	O4-H8	0.975(1)	O13-H15-O10	168.1(2)
O6-B1-O7	106.22(4)	O4-H8*	0.9940	H14-O13-H15	107.8(2)
		O4-O7	2.689(1)		
		H8-O7	1.753(1)		
		O4-H8-O7	159.6(1)		
		O4-H7	0.975(2)		
		O4-H7*	0.9946		
		O4-O12	2.809(1)		
		H7-O12	1.845(2)		
		O4-H7-O12	169.2(2)		
		H8-O4-H7	105.4(1)		

* Bond distance corrected for "riding motion" effect, following Busing and Levy (1964).

DISCUSSION AND IMPLICATIONS

The multi-methodological approach adopted to determine the chemical composition of the kurnakovite sample used in this study corroborates the general findings previously reported in the literature: the ideal formula of this borate is $\text{MgB}_3\text{O}_3(\text{OH})_5 \cdot 5\text{H}_2\text{O}$. Mg (coordination number, CN = 6) is replaced by a very modest fraction of Ca and Fe^{2+} (with $\text{CaO} + \text{FeO} < 0.06$ wt%, Tables 2 and 3); the only potential substituent of B (in CN = 4) is represented by Si (with $\text{SiO}_2 \approx 0.23$ wt%, Tables 2 and 3), though we cannot exclude that the measured fraction of Si is the effect of mineral impurities (e.g., quartz) in the massive sample of kurnakovite used for the wet chemical analysis (Tables 1 and 2). The fraction of other minor elements and of the REE is, overall, insignificant. The fluorine content, as potential OH-group substituent, is also insignificant (i.e., ~ 0.008 wt%). These experimental findings show that kurnakovite does not allow any significant isomorphic substitution. There are two principal implications of these results. First, kurnakovite cannot act as a geochemical trap of industrially relevant elements (e.g., Li, Be, or REE). Second, the almost ideal composition makes kurnakovite as a potentially good B-rich aggregate in concretes, avoiding the risk to release undesirable elements, for example, sodium, which could promote deleterious reactions for the durability of Portland or other kinds of cements.

In the framework of a long-term project to select new potential borates as B-bearing aggregates, we have reported similar findings for another mineral borate: colemanite [ideally $\text{CaB}_2\text{O}_4(\text{OH})_3 \cdot \text{H}_2\text{O}$]. Even for colemanite, no significant isomorphic substituents were found (Lotti et al. 2018, 2019). On this basis, we are inclined to consider that the unusually high level of purity is not a peculiarity of kurnakovite from the Kramer Deposit, as the colemanite that we have recently studied is from a different deposit (i.e., Bigadiç Mine, Balıkesir Province, Marmara Region, Turkey; Lotti et al. 2018, 2019). Rather, it is a common feature of the hydrous borates from lacustrine deposits with hydrothermal activity. We cannot exclude that, in such a geological environment, crystal nucleation and growth promote purification by iterated dissolution and recrystallization. However, additional evidence is needed to corroborate this potential mechanism.

The neutron structure model obtained in this study, based on intensity data collected at 293 and 20 K, is consistent with that previously reported by Corazza (1974), by single-crystal X-ray intensity data (at ambient T), and the model obtained by DFT calculation (and additional ^{11}B and ^{25}Mg NMR data) reported by Zhou et al. (2012). The structure of kurnakovite contains: $[\text{BO}_2(\text{OH})]$ -groups in triangular coordination, $[\text{BO}_2(\text{OH})_2]$ -groups in tetrahedral coordination, and $\text{Mg}(\text{OH})_2(\text{H}_2\text{O})_4$ octahedra, connected into $\text{Mg}(\text{H}_2\text{O})_4\text{B}_3\text{O}_3(\text{OH})_5$ -units forming (neutral) chains parallel to $[001]$ (Fig. 1). Chains are mutually connected to give the tri-dimensional structure only via hydrogen bonding, and extra-chains “zeolitic” H_2O molecules are also involved as “bridging molecules” (Figs. 1 and 2).

The results of the structure refinements at 293 and 20 K can be summarized as follow. (1) The triangular $[\text{BO}_2(\text{OH})]$ -group has an almost ideal configuration, with $\Delta(\text{B3-O})_{\text{max}} \sim 0.02$ Å (i.e., the difference between the longest and the shortest bond distances), O-B-O angles ranging between 117° and 123° , and aplanarity $< 2^\circ$ (here defined as the average angle described by the plane on

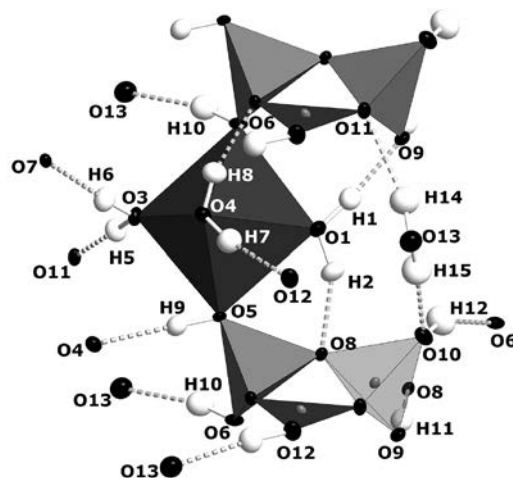


FIGURE 2. Configuration of the H-bonding network in the crystal structure of kurnakovite, based on the neutron structure refinement of this study (intensity data collected at 293 K). Displacement ellipsoid probability factor: 50%.

which the three-oxygen sites lie and each of the three independent B-O_n vectors). The tetrahedral $[\text{BO}_2(\text{OH})_2]$ -groups are only slightly distorted, but differently in magnitude, with $\Delta(\text{B1-O})_{\text{max}} \sim 0.07$ Å and $\Delta(\text{B2-O})_{\text{max}} \sim 0.03$ Å; the $\text{Mg}(\text{OH})_2(\text{H}_2\text{O})_4$ octahedron is more distorted, with $\Delta(\text{Mg-O})_{\text{max}} \sim 0.13$ Å. As expected, the B-O distances are slightly different in response to the bonding configuration of the oxygen site (i.e., oxygen of a hydroxyl group or as a bridging site between polyhedra). (2) All the oxygen sites in the structure of kurnakovite are involved in hydrogen bonding, as *donors* or *acceptors* (Table 4). (3) The four independent H_2O molecules (i.e., H3–O2–H4, H5–O3–H6, H8–O4–H7, H14–O13–H15; Table 4) show H–O–H angles ranging between 105° and 111° , still in the range of the observed H–O–H angles in solid-state materials (Chiari and Ferraris 1982; Steiner 1998 and references therein; Gatta et al. 2008, 2012, 2019; Lotti et al. 2018). The O–H distances, corrected for “riding motion effect” (following Busing and Levy 1964), range between 0.96 and 0.99 Å. All the hydrogen bonds of the H_2O molecules show O–H...O angles $\geq 156^\circ$ (Table 4), approaching an energetically favorable configuration (i.e., toward linearity, Steiner 1998), and $\text{O}_{\text{donor}} \cdots \text{O}_{\text{acceptor}}$ distances between 2.7 and 3.0 Å (Table 4). (4) The same general considerations pertaining to the H-bond configurations of the H_2O molecules can be extended to the hydroxyl groups (i.e., O1–H2, O5–H9, O6–H10, O9–H11, O10–H12, O12–H13, Table 4). All the O–H distances corrected for “riding motion effect” range between 0.96–0.99 Å, $\text{O}_{\text{donor}} \cdots \text{O}_{\text{acceptor}}$ distances range between 2.7–3.0 Å, and O–H...O $> 150^\circ$, excluding the O10–H12, which shows a bifurcated configuration with O6 and O2 as *acceptors* (with O10...O6 ~ 3.26 Å and O10–H12...O6 $\approx 157^\circ$, O10...O2 ≈ 3.07 Å and O10–H12...O2 $\approx 121^\circ$, Table 4). (5) The refinements based on the intensity data collected at 293 and 20 K provide virtually identical structure models, in terms of bond distances and angles, including the hydrogen bonds. No evidence of T -induced phase transition occurs. The main difference is on the magnitude of the atomic displacement ellipsoids: the U_{eq} values (defined as one-third of the trace

of the orthogonalized U_{ij} tensor, Supplemental¹ Tables S2 and S3) are on the average reduced by 60% at 20 K, if compared to their counterparts at 293 K. Some of the atomic displacement ellipsoids are significantly anisotropic at 293 K (Supplemental¹ Table S3, Fig. 1), but the low- T data confirm that no static or dynamic disorder occurs in the structure of kurnakovite.

The experimental findings of this study provide a comprehensive view of the important role played by the H-bonding network in the structure of kurnakovite, as expected for a material containing ~48 wt% H₂O. The three-dimensional structure of this material is basically due to the H-bonding network, providing a clue for explaining the insignificant F vs. OH substitution shown by the chemical analysis (Table 2). In such a material, we could expect that any potential structural instability in response to the change of the environmental variables (i.e., under chemical, compressional, and thermal stress conditions) would affect the H-bonding network first.

We have also calculated the bond valence (BV) sums of the cation and anion sites, based on the structural model obtained at room temperature. Mg and B sites show no significant BV sum deviations (i.e., <0.04 v.u.). More significant is the deviation for some of the O and H sites, which appear being slightly underbonded (e.g., O6, O7, O8, O9, O12, and O13 with BV sum ranging between -0.1 and -0.2 v.u.), but modeling their BV with such a complex H-bonding network is not easy. We can expect that the H-bonding scheme into the structure of kurnakovite is even more complex than that reported in Table 4, and interactions with O_{donor}...O_{acceptor} distances >3.0 Å and O_{donor}-H...O_{acceptor} angles <120°, not considered in Table 4 (298 K), could play a role, though secondary. For example, an additional weak hydrogen bond with O9 as *donor* and O1 as *acceptor* cannot be excluded, being O9...O1 = 3.366(3) Å and O9-H11...O1 = 115.1(3)° (at 298 K).

In addition to the minerogenetic conditions mentioned above, even the steric constraints in the kurnakovite structure can partially concur to its chemical purity. If we consider, for example, the 3-membered building unit made by 1[BO₂(OH)] + 2[BO₂(OH)₂]-groups (Figs. 1 and 2), a potential Si vs. B replacement (as a low fraction of Si was observed in our sample, Tables 2 and 3) at one of the tetrahedral B1 or B2 sites might drastically deform the three-membered unit and is, therefore, unlikely. We can extend the same consideration to other elements that usually occur in tetrahedral coordination at room conditions (e.g., Be, Al, P, S,...), coupled with the fact that cations with the valence number lower or higher than 3+ in any of the B-sites might, respectively under- or over-bond the bridging oxygen atoms (i.e., O5, O6, O8, O11; Figs. 1 and 2). Even the isovalent substitution of the planar [BO₂(OH)]²⁻-group with, for example, the [CO₃]²⁻-group would generate a significant chemical strain at the local scale; however, the carbon content of kurnakovite was not measured in this study (Tables 2 and 3). The octahedron could have more degrees of freedom (in terms of expansion-contraction or distortion) for isovalent substitution of Mg (e.g., with Ca or Fe²⁺), without relevant changes of its inter-polyhedral bonding configuration, mainly governed by hydrogen bonds (see Fig. 2). Overall, the planar or tetrahedral B-substitution is unlikely, but the Mg-substitution is possible and, in this respect, the high chemical purity of kurnakovite remains surprising if we do not

consider the role played by crystallization mechanisms occurring at the lacustrine deposit, described above.

These results represent the first step of a more extended study on the chemical (i.e., by leaching experiments, emulating working conditions) and physical stability (at high P and high/low T conditions) of kurnakovite to provide a comprehensive description of the behavior of this potential B-rich aggregate in Portland, Sorel, or other kinds of cements.

ACKNOWLEDGMENTS AND FUNDING

The authors thank the Institut Laue-Langevin (Grenoble, France), for the allocation of the beamtime. G.D.G. and P.L. acknowledge the support of the Italian Ministry of Education (MIUR) through the project “Dipartimenti di Eccellenza 2018–2022.” D. Zhang and M. Kunz, along with the Associate Editor O. Tschauer, are thanked for the revision of the manuscript.

REFERENCES CITED

- Archer, J., and Lehmann, M.S. (1986) A simple adjustable mount for a two-stage cryorefrigerator on an Eulerian cradle. *Journal of Applied Crystallography*, 19, 456–459.
- Busing, W.R., and Levy, H.A. (1964) The effect of thermal motion on the estimation of bond lengths from diffraction measurements. *Acta Crystallographica*, 17, 142–146.
- Carter, R.S., Palevsky, H., Myers, V.W., and Hughes, D.J. (1953) Thermal neutron absorption cross sections of boron and gold. *Physical Review*, 96, 716–721.
- Chiari, G., and Ferraris, G. (1982) The water molecules in crystalline hydrates studied by neutron diffraction. *Acta Crystallographica*, B38, 2331–2341.
- Corazza, E. (1974) The crystal structure of kurnakovite: a refinement. *Acta Crystallographica*, 30, 2194–2199.
- Di Julio, D.D., Cooper-Jensen, C.P., Perrey, H., Fissum, K., Rofors, E., Scherzinger, J., and Bentley, P.M. (2017) A polyethylene-B₂C based concrete for enhanced neutron shielding at neutron research facilities. *Nuclear Instruments Methods A*, 859, 41–46.
- Duisenberg, A.J.M. (1992) Indexing in single-crystal diffractometry with an obstatine list of reflections. *Journal of Applied Crystallography*, 25, 92–96.
- Farrugia, L.J. (1999) WinGX suite for small-molecule single-crystal crystallography. *Journal of Applied Crystallography*, 32, 837–838.
- Gatta, G.D., Rotiroli, N., McIntyre, G.J., Guastoni, A., and Nestola, F. (2008) New insights into the crystal chemistry of epididymite and eudidymite from Malosa, Malawi: a single-crystal neutron diffraction study. *American Mineralogist*, 93, 1158–1165.
- Gatta, G.D., McIntyre, G.J., Swanson, G.J., and Jacobsen, S.D. (2012) Minerals in cement chemistry: a single-crystal neutron diffraction and Raman spectroscopic study of thaumasite, Ca₃Si(OH)₄(CO₃)(SO₄)·12H₂O. *American Mineralogist*, 97, 1060–1069.
- Gatta, G.D., Lotti, P., Merlini, M., Liermann, H.-P., and Fisch, M. (2013) High-pressure behavior and phase stability of Al₃BO₆, a mullite-type ceramic material. *Journal of American Ceramic Society*, 96, 2583–2592.
- Gatta, G.D., Hälenius, U., Bosi, F., Cañadillas-Delgado, L., and Fernandez-Diaz, M.T. (2019) Minerals in cement chemistry: A single-crystal neutron diffraction study of ettringite, Ca₆Al₂(SO₄)₃(OH)₁₂·27H₂O. *American Mineralogist*, 104, 73–78.
- Glinicki, M.A., Antolik, A., and Gawlicki, M. (2018) Evaluation of compatibility of neutron-shielding boron aggregates with Portland cement in mortar. *Construction and Building Materials*, 164, 731–738.
- Larson, A.C. (1967) Inclusion of secondary extinction in least-squares calculations. *Acta Crystallographica*, 23, 664–665.
- Lotti, P., Gatta, G.D., Comboni, D., Guastella, G., Merlini, M., Guastoni, A., and Liermann, H.P. (2017) High-pressure behavior and P -induced phase transition of CaB₃O₆(OH)₂·H₂O (colemanite). *Journal of American Ceramic Society*, 100, 2209–2220.
- Lotti, P., Gatta, G.D., Demitri, N., Guastella, G., Rizzato, S., Ortenzi, M.A., Magrini, F., Comboni, D., Guastoni, A., and Fernandez-Diaz, M.T. (2018) Crystal-chemistry and temperature behavior of the natural hydrous borate colemanite, a mineral commodity of boron. *Physics and Chemistry of Minerals*, 45, 405–422.
- Lotti, P., Comboni, D., Gigli, L., Carlucci, L., Mossini, E., Macerata, E., Mariani, M., and Gatta, G.D. (2019) Thermal stability and high-temperature behavior of the natural borate colemanite: An aggregate in radiation-shielding concretes. *Construction and Building Materials*, 203, 679–686.
- Matthewman, J.C., Thompson, P., and Brown, P.J. (1982) The Cambridge Crystallography Subroutine Library. *Journal of Applied Crystallography*, 15, 167–173.
- Morgan, V., and Erd, R.C. (1969) Minerals of the Kramer borate district, California. California Division of Mines and Geology Mineral Information Service, 22, pp. 143–153 and 165–172.
- Noble, L.F. (1926) Borate deposits in the Kramer district, Kern County, California.

- U.S. Geological Survey Bulletin, 785, 45–61.
- Obert, L., and Long, A.E. (1962) Underground borate mining, Kern County, California. U.S. Bureau of Mines Report of Investigation, 6110, 1–12.
- Okuno, K., Kawai, M., and Yamada, H. (2009) Development of novel neutron shielding concrete. *Nuclear Technology*, 168, 545–552.
- Palmer, M.R., and Swihart, G.H. (1996) Boron isotope geochemistry: An overview. In L.M. Anovitz and E.S. Grew, Eds., *Boron: Mineralogy, Petrology, and Geochemistry*, 33, pp. 709–744. Review in *Mineralogy*, Mineralogical Society of America, Chantilly, Virginia.
- Petch, H.E., Pennington, K.S., and Cuthbert, J.D. (1962) On Christ's postulated boron-oxygen polyions in some hydrated borates of unknown crystal structure. *American Mineralogist*, 47, 401–404.
- Puffer, J.H. (1975) The Kramer borate mineral assemblage. *Mineralogical Record*, 6, 84–91.
- Rauch, H., and Waschkowski, W. (2002) Neutron scattering lengths. In A.J. Dianoux and G. Lander, Eds., *Neutron Data Booklet*, first ed., pp. 1–18. Institut Laue Langevin, Grenoble.
- Razmanova, Z.P., Rumonova, I.M., and Belov, N.V. (1969) Crystalline structure of kurnakovite $Mg_3B_6O_{11} \cdot 15H_2O = 2Mg[B_3O_3(OH)_5] \cdot 5H_2O$. *Soviet Physics "Doklady" (English Transl.)*, 14, 1139–1142.
- Schaller, W. (1930) Borate minerals from the Kramer district, Mohave Desert, California. U.S. Geological Survey Professional Paper, 158, 137–170.
- Sears, V.F. (1986) Neutron scattering lengths and cross-sections. In K. Sköld and D.L. Price, Eds., *Neutron Scattering, Methods of Experimental Physics*, 23A, pp. 521–550. Academic Press.
- Sheldrick, G.M. (1997) SHELXL-97. Programs for crystal structure determination and refinement. University of Göttingen, Germany.
- (2008) A short history of SHELX. *Acta Crystallographica*, A64, 112–122.
- Siefke, J.W. (1991) The Boron open Pit Mine at the Kramer Borate Deposit. The Diversity of Mineral and Energy Resources of Southern California. In M.A. McKibben, Ed., *Society of Economic Geologists Guidebook Series*, 12, p. 4–15.
- Steiner, T. (1998) Opening and narrowing of the water H-O-H angle by hydrogen-bonding effects: Re-inspection of neutron diffraction data. *Acta Crystallographica*, B54, 464–470.
- Whistler, D.P. (1984) An early Hemingfordian (Early Miocene) fossil vertebrate fauna from Boron, Western Mojave Desert, California. *Contributions in Science*, 355, 36 pp.
- Wilkinson, C., Khamis, H.W., Stansfield, R.F.D., and McIntyre, G.J. (1988) Integration of single-crystal reflections using area multidetectors. *Journal of Applied Crystallography*, 21, 471–478.
- Zhou, B., Michaelis, V.K., Pan, Y., Yao, Y., Tait, K.T., Hyde, B.C., Wren, J.E.C., Sherriff, B.L., and Kroeker, S. (2012) Crystal structure refinements of borate dimorphs inderite and kurnakovite using ^{11}B and ^{25}Mg nuclear magnetic resonance and DFT calculations. *American Mineralogist*, 97, 1858–1865.

MANUSCRIPT RECEIVED MARCH 31, 2019

MANUSCRIPT ACCEPTED JUNE 15, 2019

MANUSCRIPT HANDLED BY OLIVER TSCHAUNER

Endnote:

¹Deposit item AM-19-97072, CIF and Supplemental Tables S1–S3. Deposit items are free to all readers and found on the MSA website, via the specific issue's Table of Contents (go to http://www.minsocam.org/MSA/AmMin/TOC/2019/Sep2019_data/Sep2019_data.html).